

## Snapshots of a Metamorphosing Cu(II) Ground State in a Galactose Oxidase-Inspired Complex

Russell C. Pratt, Liviu M. Mirica, and T. Daniel P. Stack\*

Department of Chemistry, Stanford University, Stanford, California 94305

Received August 9, 2004

The novel ligand 2,6-bis[*S*-(3,5-di-*tert*-butyl-2-hydroxyphenyl)sulfanylmethyl]pyridine (**H<sub>2</sub>L1**) and its copper(II) complex Cu(**L1**), **1**, were synthesized with the aim of constructing a model of the active site of the enzyme galactose oxidase (GOase). Cyclic voltammetry studies show that **1** undergoes ligand-based quasi-reversible oxidations (phenolate/phenoxy) and reversible metal-based reduction [copper(II)/copper(I)] similar to those of GOase, but at potentials much higher and lower, respectively, than those found for the enzyme. At room temperature, spectrophotometric titrations show that **1** binds strongly to 1 equiv of pyridine. In frozen solutions (77 K), **1** quantitatively binds both pyridine and ethers (e.g., 1,4-dioxane) as assessed by X- and Q-band EPR spectroscopy. Profound shifts in the pattern of *g* values result, from rhombic ( $g_1 > g_2 > g_3$ ) in toluene to either inverted axial patterns ( $g_1 = g_2 \gg g_3$ ) in the presence of ethers or a near-axial pattern ( $g_1 \gg g_2 > g_3$ ) in the presence of pyridine. Crystallographic analyses of the parent complex **1**·MeCN, the dioxane-bridged dimer [(Cu(**L1**))<sub>2</sub>(( $\mu$ -1,4)-1,4-dioxane)]·(Me<sub>2</sub>CO)<sub>2</sub> (**2**), and the pyridine complex [Cu(**L1**)(pyridine)] (**3**) show that the pyridine and ether ligands bond to copper at a sixth octahedral position left vacant by the pentadentate NO<sub>2</sub>S<sub>2</sub> coordination mode of **L1**<sup>2-</sup> and induce perturbations of its geometry. Hybrid DFT calculations based on the crystallographic coordinates combined with perturbation theory expressions for the *g* values of a d<sup>9</sup> system correlate the results from EPR spectroscopy to the proportions of d<sub>x<sup>2</sup>-y<sup>2</sup></sub> and d<sub>z<sup>2</sup></sub> character in the relevant copper-centered unoccupied molecular orbital. The combination of spectroscopic, structural, and computational results for this set of copper(II) complexes provides a demonstrative example of the physical phenomena underlying rhombic EPR spectra of d<sup>9</sup> systems.

### Introduction

The mononuclear copper enzyme galactose oxidase (GOase) catalyzes the selective oxidation of primary alcohols to aldehydes by dioxygen, which is reduced to hydrogen peroxide (Figure 1).<sup>1</sup> In addition to the copper atom, the active site of GOase contains a copper-bound, cysteine-linked tyrosine residue that operates as an additional one-electron cofactor shuttling between either tyrosine or tyrosinate and tyrosyl radical forms. The two cofactors operate in tandem to accomplish substrate-oxidizing and dioxygen-reducing half-reactions in a ping-pong mechanism that takes the enzyme between fully oxidized copper(II) tyrosyl and fully reduced copper(I) tyrosin(at)e forms (GOase<sub>ox</sub> and GOase<sub>red</sub>, respectively). Importantly, GOase in its intermediate copper(II) tyrosinate oxidation state (GOase<sub>semi</sub>) is inactive and must

be oxidized to GOase<sub>ox</sub> ( $E^{\circ'} = +400$  mV vs NHE, pH 7.5) or reduced to GOase<sub>red</sub> ( $E^{\circ'} = +150$  mV) to enter the catalytic cycle.<sup>2,3</sup>

Many groups have constructed small-molecule models of the active site of GOase.<sup>4</sup> The result is a plethora of structural variants and spectroscopic analogues of GOase<sub>ox</sub> that mimic its phenoxy  $\pi$ - $\pi^*$  absorptions in the near-UV region, its broad CT features in the vis-NIR region, and its featureless EPR spectrum arising from antiferromagnetic exchange between Cu<sup>II</sup> and the tyrosyl radical.<sup>1</sup> Modeling studies have also attempted to duplicate the reactivity of GOase. Successful single-turnover experiments have provided mechanistic insight into the hydrogen-atom-abstraction activity of copper-coordinated phenoxy radicals.<sup>5-8</sup> In some cases, catalytic alcohol oxidation was achieved using copper

\* To whom correspondence should be addressed. E-mail: stack@stanford.edu.

(1) Whittaker, J. W. *Chem. Rev.* **2003**, *103*, 2347–2363.

(2) Whittaker, M. M.; Whittaker, J. W. *J. Biol. Chem.* **1988**, *263*, 6074–6080.

(3) Wright, C.; Sykes, A. G. *J. Inorg. Biochem.* **2001**, *85*, 237–243.

(4) Jazdzewski, B. A.; Tolman, W. B. *Coord. Chem. Rev.* **2000**, *200*, 633–685.

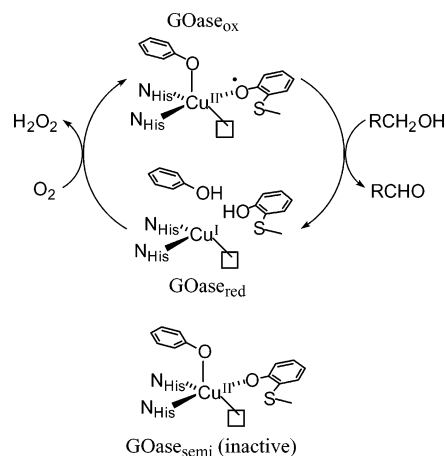


**Figure 1.** Consensus reaction mechanism of GOase, showing alternation between fully oxidized (GOase<sub>ox</sub>) and fully reduced (GOase<sub>red</sub>) active forms, and the semi-oxidized, inactive form of the enzyme (GOase<sub>semi</sub>). Both the oxidizing and reducing half-reactions require transfer of two electrons and two protons.

phenolate complexes in the presence of strong bases and oxygen, but the complicated, basic reaction conditions do not allow the integrity or nature of the active catalyst to be verified.<sup>9–11</sup> There does exist a distinct class of three heteroatom-bridged diphenolate ligands developed by Chaudhuri et al. whose copper complexes have both single-turnover activity and catalytic activity under very mild conditions; the complex based on bis(3,5-di-*tert*-butyl-2-hydroxyphenyl)-amine in particular operates by a mechanism with high fidelity to that of GOase.<sup>12–14</sup>

We recently reported copper phenolate/phenoxy complexes based on salen-type ligands that provide interesting spectroscopic and mechanistic results in modeling GOase<sub>ox</sub> and the substrate-oxidizing half-reaction.<sup>15</sup> However, their use in fully duplicating the reactivity of GOase is limited to 2:1 stoichiometry in the oxidation of benzyl alcohol, apparently because of their inability to form stable Cu<sup>I</sup> complexes. To achieve catalytic, aerobic oxidation of alcohols, new ligands are needed to overcome this inherent limitation. The unique cofactor of GOase itself suggested an approach, as the cysteine–tyrosine link in GOase forms a thioether. In

the enzyme, donation of electron density from the thioether allows easier oxidation of the cofactor, thereby aiding catalytic turnover.<sup>3</sup> From the point of view of a coordination chemist, a thioether is a soft ligand that favors lower oxidation states of metals, such as Cu<sup>I</sup>.<sup>16</sup> Inclusion of an *ortho*-alkylsulfanyl substituent on a phenolate moiety therefore offers the possibility of both donating electron density into the aromatic ring, making it easier to oxidize to a phenoxy radical, and also chelating the copper with a thioether, making it easier to reduce to a Cu<sup>I</sup> species.

Of the few reported examples of transition metal complexes with chelating *ortho*-alkylsulfanylphenolates, most are reported in the context of GOase modeling. An early model lacked substituents on the chelating sulfanylphenolate necessary for stabilizing an oxidized phenoxy derivative but demonstrated O,S chelation.<sup>17</sup> More recently, a series of Cu<sup>II</sup> complexes with chelating *ortho*-thioetherphenolates was reported, but oxidation of the phenolates is irreversible in all cases.<sup>18</sup> Shortly thereafter, two Ti<sup>IV</sup> complexes of similar ligands were described as olefin polymerization catalysts.<sup>19</sup> In this last study, the ligands were synthesized from 4,6-di-*tert*-butyl-2-mercaptophenol and alkyl halides by nucleophilic substitution, and we also adopted this method as a procedurally simple and versatile means of constructing ligands.<sup>20</sup>

Ultimately, we identified H<sub>2</sub>L1 as a new ligand suited for coordination to Cu<sup>II</sup>. Coordination of this ligand was expected to resemble that of other NS<sub>2</sub> pincer-type ligands, with the sulfur-linked phenolates providing additional denticity.<sup>21–24</sup> Herein is described the synthesis and characterization of the complex Cu(L1), **1**, and a brief evaluation of its ability to electrochemically form analogues of all three oxidation states of GOase. Also, we have found that **1** has interesting interactions with additional monodentate ligands and have correlated spectroscopic, structural, and computational results to examine the effects of these added ligands on the Cu<sup>II</sup> ground state in **1**.

## Experimental Section

**Materials and Methods.** Solvents and starting materials were purchased from commercial sources and used without purification unless otherwise noted. <sup>1</sup>H NMR spectra were acquired for CDCl<sub>3</sub> solutions using a Varian XL-400 spectrometer operating at 400 MHz. EPR spectra were collected using a Bruker EMX spectrometer; X-band spectra were measured using an ER041XG microwave

- (5) Halfen, J. A.; Young, V. G.; Tolman, W. B. *Angew. Chem., Int. Ed. Engl.* **1996**, *35*, 1687–1690.
- (6) Itoh, S.; Taki, M.; Takayama, S.; Nagatomo, S.; Kitagawa, T.; Sakurada, N.; Arakawa, R.; Fukuzumi, S. *Angew. Chem., Int. Ed.* **1999**, *38*, 2774–2776.
- (7) Saint-Aman, E.; Menage, S.; Pierre, J. L.; Defrancq, E.; Gellon, G. *New J. Chem.* **1998**, *22*, 393–394.
- (8) Sénèque, O.; Campion, M.; Douziche, B.; Giorgi, M.; Le Mest, Y.; Renaud, O. *Dalton Trans.* **2003**, 4216–4218.
- (9) Thomas, F.; Gellon, G.; Gautier-Luneau, I.; Saint-Aman, E.; Pierre, J.-L. *Angew. Chem., Int. Ed.* **2002**, *41*, 3047–3050.
- (10) Wang, Y.; DuBois, J. L.; Hedman, B.; Hodgson, K. O.; Stack, T. D. P. *Science* **1998**, *279*, 537–540.
- (11) Kitajima, N.; Whang, K.; Moro-Oka, Y.; Uchida, A.; Sasada, Y. *J. Chem. Soc., Chem. Commun.* **1986**, 1504–1505.
- (12) Chaudhuri, P.; Hess, M.; Florke, U.; Wieghardt, K. *Angew. Chem., Int. Ed.* **1998**, *37*, 2217–2220.
- (13) Chaudhuri, P.; Hess, M.; Weyhermüller, T.; Wieghardt, K. *Angew. Chem., Int. Ed.* **1999**, *38*, 1095–1098.
- (14) Chaudhuri, P.; Hess, M.; Müller, J.; Hildenbrand, K.; Bill, E.; Weyhermüller, T.; Wieghardt, K. *J. Am. Chem. Soc.* **1999**, *121*, 9599–9610.
- (15) Pratt, R. C.; Stack, T. D. P. *J. Am. Chem. Soc.* **2003**, *125*, 8716–8717.

- (16) Cotton, F. A.; Wilkinson, G. *Advanced Inorganic Chemistry*, 5th ed.; Wiley-Interscience: New York, 1988.
- (17) Ruf, M.; Pierpont, C. G. *Angew. Chem., Int. Ed.* **1998**, *37*, 1736–1739.
- (18) Kruse, T.; Weyhermüller, T.; Wieghardt, K. *Inorg. Chim. Acta* **2002**, *331*, 81–89.
- (19) Capacchione, C.; Proto, A.; Ebeling, H.; Mülhaupt, R.; Möller, K.; Spaniol, T. P.; Okuda, J. *J. Am. Chem. Soc.* **2003**, *125*, 4964–4965.
- (20) Kuliev, A. M.; Farzaliev, V. M.; Allakhverdiev, M. A.; Mamedov, C. I. *Zh. Obshch. Khim.* **1982**, *52*, 2122–2126.
- (21) Teixidor, F.; Escriche, L.; Alegret, S.; Jaime, C.; Pérez-Jiménez, C.; Mestres, L.; Rius, J.; Molins, E.; Miravittles, C.; Teixidor, F. *Inorg. Chem.* **1991**, *30*, 1893–1898.
- (22) Escriche, L.; Sanz, M.; Casabó, J.; Teixidor, F.; Molins, E.; Miravittles, C. *J. Chem. Soc., Dalton Trans.* **1989**, 1739–1743.
- (23) Teixidor, F.; Sánchez-Castelló, G.; Lucena, N.; Escriche, L.; Kivekäs, R.; Sundberg, M.; Casabó, J. *Inorg. Chem.* **1991**, *30*, 4931–4935.
- (24) Masuda, H.; Sugimori, T.; Kohzuma, T.; Odani, A.; Yamauchi, O. *Bull. Chem. Soc. Jpn.* **1992**, *65*, 786–793.

bridge and an ER4102ST cavity, with samples held in a liquid-nitrogen-filled finger Dewar; Q-band spectra were measured using an ER051QR microwave bridge, an ER5106QT resonator, and an Oxford continuous-flow CF935 cryostat. EPR  $g$  values were referenced to DPPH ( $g = 2.0036$ ) or quartz ( $g = 2.0023$ ). UV-vis spectroscopy was performed using a Cary 50 or Cary 500 dual-beam spectrophotometer. Electrochemical experiments were performed in  $\text{CH}_2\text{Cl}_2$  with 0.1 M tetrabutylammonium perchlorate as the supporting electrolyte, using a BAS CV-50 potentiometer and a cell equipped with a AgCl/Ag reference electrode, a glassy carbon working electrode, and a platinum counter electrode. Decamethylferrocene was used as an internal reference ( $-530$  mV vs  $\text{Fc}^+/\text{Fc}$ ). Mass spectrometry was performed by Stanford Mass Spectrometry Services (Stanford, CA). Analytical services were provided by Desert Analytics (Tucson, AZ).

**Syntheses.** (i) **4,6-Di-*tert*-butyl-2-mercaptophenol.** This compound was synthesized by a modified literature procedure.<sup>20</sup> To a solution of 2,4-di-*tert*-butylphenol (1.03 g, 5.0 mmol) in benzene (10 mL) was added  $\text{S}_2\text{Cl}_2$  (400  $\mu\text{L}$ , 0.675 g, 5.0 mmol). The solution was stirred and heated gently (50 °C) for 1 h. Granulated zinc (5.0 g) and concentrated hydrochloric acid (5 mL) were then added, and the resulting mixture was heated to reflux for 2 h. Excess Zn was removed by filtration, and the organic layer was washed repeatedly with water until the washings were neutral. The organic layer was then dried with  $\text{MgSO}_4$  and filtered, and the solvent was removed under reduced pressure to give a white solid that was used without further purification. Yield: 1.13 g (95%).  $^1\text{H NMR}$ :  $\delta$  7.41 (m, 1H, ArH), 7.33 (m, 1H, ArH), 6.67 (s, 1H, OH), 2.87 (s, 1H, SH), 1.44 (s, 9H, *tert*-Bu), 1.31 (s, 9H, *tert*-Bu).

(ii) **2,6-Bis[S-(3,5-di-*tert*-butyl-2-hydroxyphenyl)sulfanyl-methyl]pyridine (**H<sub>2</sub>L1**).** 2,6-Di(chloromethyl)pyridine (194 mg, 1.1 mmol) and 4,6-di-*tert*-butyl-2-mercaptophenol (522 mg, 2.2 mmol) were dissolved in deoxygenated ethanol (11 mL), and ethanolic sodium hydroxide (0.2 M, 11 mL, 2.2 mmol) and water (2 mL) were then added. The precipitate subsequently formed was isolated by filtration and dried under reduced pressure, giving a white solid that was used without further purification. Yield: 540 mg (85%).  $^1\text{H NMR}$ :  $\delta$  8.34 (s, 2H, ArH), 7.34 (t, 1H, *p*-PyH), 7.29 (s, 4H?), 6.73 (d, 2H, *m*-PyH), 4.05 (s, 4H,  $\text{CH}_2$ ), 1.36 (s, 18H, *tert*-Bu), 1.26 (s, 18H, *tert*-Bu). ESI-MS: 580 (M+1).

(iii) **1·MeCN.** To a stirred solution of **H<sub>2</sub>L1** (500 mg, 0.85 mmol) in 1:1 (v/v) methanol/tetrahydrofuran (30 mL) were added  $\text{Cu}(\text{OAc})_2 \cdot \text{H}_2\text{O}$  (170 mg, 0.85 mmol) and methanolic sodium hydroxide (0.2 M, 8.5 mL, 1.7 mmol). Once all solids had dissolved, the solvent was removed under reduced pressure, and the residues were extracted with acetonitrile (total volume 40 mL) and then filtered. Addition of water (5 mL) followed by slow evaporation yielded black, blocky crystals that were isolated by filtration and dried in vacuo. Yield: 320 mg (55%). Calcd (found) for  $\text{C}_{37}\text{H}_{50}\text{CuN}_2\text{O}_2\text{S}_2$ : C 65.11 (65.39), H 7.38 (7.71), N 4.10 (4.17), S 9.40 (9.35). ESI-MS (acetone):  $m/z$  641 (M + 1).

(iv) **1<sub>2</sub>( $\mu$ -1,4)-1,4-dioxane)·(Me<sub>2</sub>CO)<sub>2</sub> [2·(Me<sub>2</sub>CO)<sub>2</sub>].** Slow evaporation of a solution of 1·MeCN (34 mg, 50  $\mu\text{mol}$ ) in 9:1:1 (v/v/v) acetone/1,4-dioxane/water yielded red plates. Yield: 25 mg (65%). Calcd (found) for  $\text{C}_{80}\text{H}_{114}\text{Cu}_2\text{N}_2\text{O}_8\text{S}_4$ : C 64.61 (64.64), H 7.73 (7.93), N 1.88 (2.08), S 8.62 (8.34). ESI-MS (acetone + 10% 1,4-dioxane):  $m/z$  641 (M(1) + 1).

(v) **1(pyridine) (3).** Slow evaporation of a solution of 1·MeCN (34 mg, 50  $\mu\text{mol}$ ) in 20:1.5:1 (v/v/v) methanol/pyridine/water (10 mL) yielded brown needles. Yield: 25 mg (70%). Calcd (found) for  $\text{C}_{40}\text{H}_{52}\text{CuN}_2\text{O}_2\text{S}_2$ : C 66.68 (66.54), H 7.27 (7.09), N 3.89 (3.95), S 8.90 (8.62). ESI-MS (acetone + 10% pyridine):  $m/z$  641 (M(1) + 1).

**X-ray Crystallography.** Crystals of 1·MeCN, 2·(Me<sub>2</sub>CO)<sub>2</sub>, or 3 were mounted in Paratone N oil on quartz fibers. All measurements were made on a Bruker-Siemens SMART<sup>25</sup> CCD area detector with graphite-monochromated Mo  $K\alpha$  radiation. Data were collected using the  $\omega$  scan technique to a maximum  $2\theta$  value of 49.4°. Frames corresponding to an arbitrary hemisphere of data were collected using  $\omega$  scans of 0.3°, counted for a total of 10 s per frame. Data were analyzed for agreement and possible absorption using SADABS.<sup>26</sup> The data were corrected for Lorentz and polarization effects. No decay correction was applied. The structures were solved by direct methods and expanded using Fourier techniques. The non-hydrogen atoms were refined anisotropically. Most hydrogen atoms were located by difference Fourier synthesis but were fixed at idealized positions.

Wide ranges of observed atomic  $U_{\text{eq}}$  values reflect the contrast in thermal lability between relatively rigid ligand backbone atoms and less conformationally restricted atoms in the ligand *tert*-butyl substituents and noncoordinating solvates when present. Solvent-accessible voids (40–50 Å<sup>3</sup>) were present in the final models of the unit cells of 1·MeCN and 2·(Me<sub>2</sub>CO)<sub>2</sub>. Preliminary analyses using the BYPASS (SQUEEZE) procedure of van der Sluis and Spek<sup>27,28</sup> suggested the presence of one to two and four to five electrons within each of these voids, respectively; however, the residual density was ill-defined on the Fourier map and was left unmodeled. Refinement of the model against solvent-free data obtained from the SQUEEZE algorithm did not afford significant improvement in the weighted  $R$  factor. Mean-square displacement amplitude (MSDA) analyses of the coordination spheres of 1–3 do not show evidence of dynamic disorder in the crystal structures.<sup>29,30</sup>

Neutral-atom scattering factors were taken from Cromer and Waber.<sup>31</sup> Anomalous dispersion effects were included in  $F_c$ ;<sup>32</sup> the values for  $\Delta f'$  and  $\Delta f''$  were those of Creagh and McAuley.<sup>33</sup> The values for the mass attenuation coefficients are those of Creagh and Hubbell.<sup>34</sup> All calculations were performed using the Crystal-Structure crystallographic software package except for refinement, which was performed using SHELXL-97.

**Computational Studies.** DFT calculations were performed with the program package Gaussian 98.<sup>35</sup> On the basis of the crystallographic coordinates of 1–3 with solvate molecules excluded, single-point calculations were performed using a spectroscopically calibrated hybrid functional with 38% Hartree–Fock exchange added to the BP86 functional.<sup>36</sup> A general basis set (6-311G\* for Cu and 6-31G\* for all other atoms) was used for all Gaussian calculations, and atomic orbital compositions were calculated using AOMix.<sup>37</sup>

The wave functions obtained for the ground states were investigated by analyzing the highest occupied molecular orbitals

(25) SMART: Area-Detector Software Package; Siemens Industrial Automation, Inc.: Madison, WI, 1995.

(26) SADABS: Siemens Area Detector Absorption Correction Program, version 2.05; Bruker AXS Inc.: Madison, WI, 1998.

(27) Spek, A. J. *Appl. Crystallogr.* **2003**, *36*, 7–13.

(28) van der Sluis, P.; Spek, A. L. *Acta Crystallogr. A* **1990**, *46*, 194–201.

(29) Falvello, L. R. *Dalton Trans.* **1997**, 4463–4475.

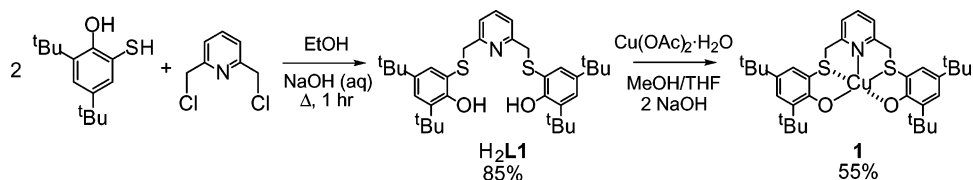
(30) Halcrow, M. A. *Dalton Trans.* **2003**, 4375–4384.

(31) Cromer, D. T.; Waber, J. T. *International Tables for X-ray Crystallography*; Kynoch: Birmingham, AL, 1974; Vol. IV.

(32) Ibers, J. A.; Hamilton, W. C. *Acta Crystallogr.* **1964**, *17*, 781–782.

(33) Creagh, D. C.; McAuley, W. J. In *International Tables for Crystallography*; Wilson, A. J. C., Ed.; Kluwer Academic Publishers: Boston, 1992; Vol. C, pp 219–222, Table 4.2.6.8.

(34) Creagh, D. C.; Hubbell, J. H. In *International Tables for Crystallography*; Wilson, A. J. C., Ed.; Kluwer Academic Publishers: Boston, 1992; Vol. C, pp 200–206 Table 4.2.4.3.

Scheme 1. Synthesis of H<sub>2</sub>L1 and 1

(HOMOs), the lowest unoccupied molecular orbitals (LUMOs), and the Cu-based molecular orbitals (MOs) that showed predominantly d character. Spin-unrestricted calculations were needed to obtain a reasonable spin density on the Cu center. Each molecular orbital was differentiated into  $\alpha$  and  $\beta$  components, according to the spin of the electrons. For the spectroscopically relevant lowest unoccupied molecular orbital with predominant Cu character, the  $\beta$  component was analyzed, representing the electron hole at the Cu center.

The  $z$  matrices were carefully chosen to orient the d manifold of Cu as closely as possible with the Cu–ligand bonds and thereby minimize linear combination and/or transformation of the d orbitals that would mask the actual orbital mixing. Two coordinate systems were used:  $xyz$ , in which the NO<sub>2</sub> atoms of **L1**<sup>2-</sup> occupy the  $xy$  plane and the Cu–S bonds are oriented as closely as possible along the  $z$  axis, and  $x'y'z'$ , in which the Cu–N(**L1**) bond coincides with the  $z$  axis and the O<sub>2</sub>S<sub>2</sub> atoms roughly occupy the  $x'y'$  plane (see also Figure 9).

## Results

**Synthesis of 1.** The synthesis of **1** is summarized in Scheme 1. Following a literature procedure for the synthesis of 4,6-di-*tert*-butyl-2-mercaptophenol by treating 2,4-di-*tert*-butylphenol with the theoretical minimum of 0.5 equiv of S<sub>2</sub>Cl<sub>2</sub> gave not only the desired product but also bis(3,5-di-*tert*-butyl-2-hydroxyphenyl)sulfide as a byproduct that was difficult to remove.<sup>20</sup> Use of 1 equiv of S<sub>2</sub>Cl<sub>2</sub> per equivalent of phenol avoided formation of the byproduct and gave the desired mercaptophenol in high yields (>90%). The efficacy and regiochemistry of 4,6-di-*tert*-butyl-2-mercaptophenol as a sulfur nucleophile has been previously demonstrated,<sup>19,20</sup> and its reaction with 2,6-di(chloromethyl)pyridine led to H<sub>2</sub>L1 in useful yields. Metalation of H<sub>2</sub>L1 using Cu(OAc)<sub>2</sub>·H<sub>2</sub>O and base provided **1** as a purple solid that is soluble in most solvents, the only known exceptions being water and dimethyl sulfoxide. Recrystallization of **1** by slow evaporation of acetonitrile/water solutions gave **1**·MeCN as purple-black crystals in acceptable yields and purity.

**Electrochemistry.** Cyclic voltammograms of CH<sub>2</sub>Cl<sub>2</sub>/0.1 M Bu<sub>4</sub>N<sup>+</sup>ClO<sub>4</sub><sup>-</sup> solutions of **1** show overlapping, quasi-

reversible oxidations ( $i_a/i_c < 1$ ) at potentials of +470 and +620 mV versus Fc<sup>+</sup>/Fc (Figure 2). These processes are assigned to sequential oxidations of the two phenolate moieties and occur at slightly lower potentials than those previously found for chelating *ortho*-sulfanylphenolate complexes. An additional feature uncommonly cited for GOase model complexes is a reversible reduction ( $i_a/i_c \approx 1$ ) observed at -1230 mV, assigned to the Cu<sup>II</sup>/Cu<sup>I</sup> couple. A large separation of the cathodic and anodic half-waves of the reduction ( $\Delta E_{p-p} = 180$  mV; cf.  $\Delta E_{p-p} = 75$  mV for the internal reference) indicates that some rearrangement might occur upon reduction/oxidation to accommodate the different geometrical preferences of Cu<sup>I</sup> and Cu<sup>II</sup> ions.<sup>38</sup>

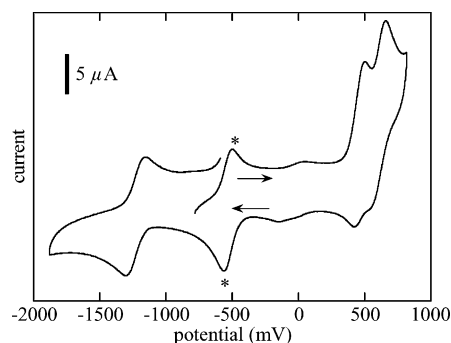


**Figure 2.** Cyclic voltammogram of **1**. Peaks marked with an asterisks (\*) are due to the internal reference (decamethylferrocene). Conditions: 0.1 M Bu<sub>4</sub>NClO<sub>4</sub> in CH<sub>2</sub>Cl<sub>2</sub>, scan rate 100 mV/s, potentials referenced to Fc<sup>+</sup>/Fc = 0 mV.

Attempts to generate a solution of the one-electron-oxidized form of **1** by treatment with thianthrenyl radical cation ( $E^\circ = +890$  mV)<sup>39</sup> at room temperature in CH<sub>2</sub>Cl<sub>2</sub> resulted in irreversible decomposition of the complex; reverse titrations with reductant (Fc) did not restore the spectrum of **1**. The oxidation is only quasi-reversible even on the time scale of cyclic voltammetry, so the instability is not unexpected. Attempts to form **1**<sup>-</sup> (i.e. [Cu<sup>I</sup>L1]<sup>-</sup>) by complexation of Cu<sup>I</sup> salts have not succeeded: typically a purple solution indicative of neutral **1** results.

**UV–Vis Spectroscopy and Binding of Neutral Ligands.** H<sub>2</sub>L1 is a white solid, and solutions of H<sub>2</sub>L1 in toluene show no absorption maxima at wavelengths longer than 300 nm. In toluene solution, **1** shows electronic absorption features at 311 ( $\epsilon = 10\,500$  M<sup>-1</sup> cm<sup>-1</sup>), 337 (10 500), 557 (1050), and 988 nm (190). The UV absorptions can be assigned to endogenous pyridyl and thioether ligand-to-metal charge-transfer (LMCT) bands on the basis of their energies and intensities.<sup>40</sup> Because of its high intensity, the visible

(35) Frisch, M. J.; Trucks, G. W.; Schlegel, H. B.; Scuseria, G. E.; Robb, M. A.; Cheeseman, J. R.; Zakrzewski, V. G.; Montgomery, J. A., Jr.; Stratmann, R. E.; Burant, J. C.; Dapprich, S.; Millam, J. M.; Daniels, A. D.; Kudin, K. N.; Strain, M. C.; Farkas, O.; Tomasi, J.; Barone, V.; Cossi, M.; Cammi, R.; Mennucci, B.; Pomelli, C.; Adamo, C.; Clifford, S.; Ochterski, J.; Petersson, G. A.; Ayala, P. Y.; Cui, Q.; Morokuma, K.; Malick, D. K.; Rabuck, A. D.; Raghavachari, K.; Foresman, J. B.; Cioslowski, J.; Ortiz, J. V.; Stefanov, B. B.; Liu, G.; Liashenko, A.; Piskorz, P.; Komaromi, I.; Gomperts, R.; Martin, R. L.; Fox, D. J.; Keith, T.; Al-Laham, M. A.; Peng, C. Y.; Nanayakkara, A.; Gonzalez, C.; Challacombe, M.; Gill, P. M. W.; Johnson, B. G.; Chen, W.; Wong, M. W.; Andres, J. L.; Head-Gordon, M.; Replogle, E. S.; Pople, J. A. *Gaussian 98*, revision A.11.2; Gaussian, Inc.: Pittsburgh, PA, 1998.

(36) Szilagy, R. K.; Metz, M.; Solomon, E. I. *J. Phys. Chem. A* **2002**, *106*, 2994–3007.

(37) Gorelsky, S. I.; Lever, A. B. P. *AOMix*, revision 4.7; York University: Ontario, Canada, 2001.

(38) Rorabacher, D. B. *Chem. Rev.* **2004**, *104*, 651–697.

(39) Connelly, N. G.; Geiger, W. E. *Chem. Rev.* **1996**, *96*, 877–910.

(40) Lever, A. D. P. *Inorganic Electronic Spectroscopy*; 2nd ed.; Elsevier: Amsterdam, 1984.

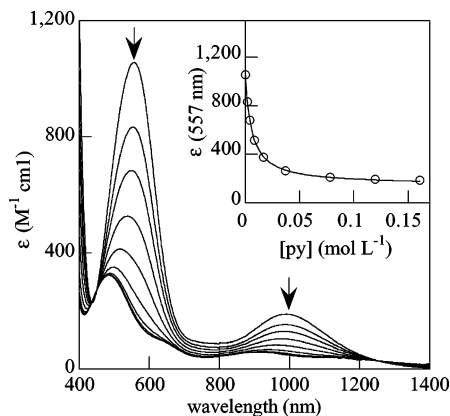
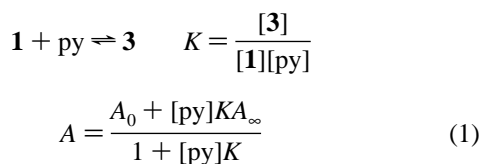


**Figure 3.** UV–vis titration of **1** (1.0 mM) with pyridine in toluene at 25 °C. Inset: Trace of the absorbance at 557 nm vs concentration of pyridine, shown with a fit generated by eq 1.

absorption responsible for the deep purple color of **1** is most likely a phenolate–copper LMCT, whereas the NIR absorption is assigned to d–d transitions.<sup>40</sup>

As the coordination about copper in **1** is pentadentate, it was anticipated that a sixth site on the copper would be accessible to additional ligands. Indeed, addition of excess pyridine to toluene solutions of **1** at room temperature causes a color change from deep purple to pale red, indicating formation of a new species. A spectrophotometric titration of **1** with pyridine in toluene (Figure 3) shows the decrease in the intensity of the visible absorption. Fitting of the spectral trace at 557 nm with eq 1 (Figure 3, inset), where  $A$  is the absorbance of the solution;  $A_0$  and  $A_\infty$  are the initial and final absorbances, respectively; and terms in square brackets refer to molar concentrations, gives a constant of  $K = 150 \pm 20 \text{ M}^{-1}$  for addition of a single pyridine molecule at 25 °C in toluene.



The absorption features of this new species are at 317 ( $\epsilon = 15\,000$ ), 485 (300), 658 (sh), 909 (60), and 1250 nm (sh). The weak, low-energy bands are assigned to d–d transitions.<sup>40</sup> Notably, only one LMCT absorption remains in the UV region. Given that a pyridine has been added to the complex, it is more likely that the pyridine–copper LMCT remains (317 nm) and the thioether–copper LMCT is buried or lost.

**EPR Spectroscopy.** The X-band and Q-band EPR spectra of **1** in frozen toluene (77 K) are distinctly rhombic ( $g_1 > g_2 > g_3$ , Figures 4a and 5a) and could be simulated using parameters listed in Table 1. The same rhombic EPR spectra were also obtained for frozen solutions of **1** in acetone and acetonitrile, and a broadened rhombic spectrum was acquired for a solution of **1** in methylene chloride.

Following from the UV–vis study of pyridine addition to toluene solutions, inclusion of pyridine (1–10%, v/v) also affects the frozen solution spectrum of **1** (Figures 4c and

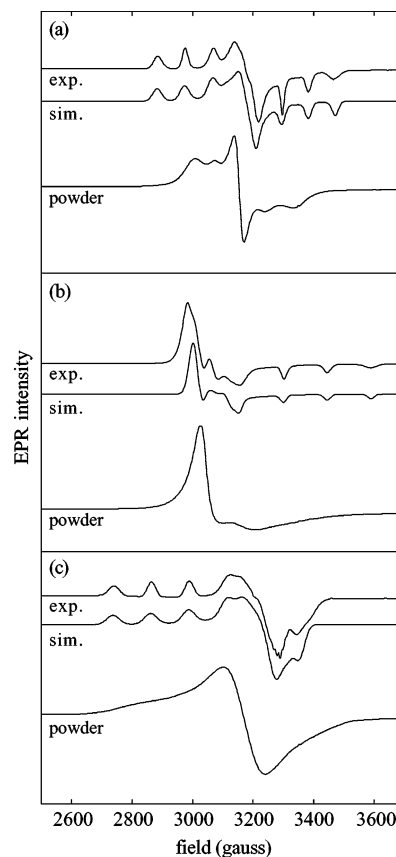


**Figure 4.** Experimental and simulated X-band EPR spectra of frozen (77 K)  $\sim 1$  mM solutions of **1** in (a) toluene, (b) 9:1 toluene/1,4-dioxane, and (c) 99:1 toluene/pyridine. Also shown are powder spectra for solid samples of (a) **1**·MeCN, (b) **2**·(Me<sub>2</sub>CO)<sub>2</sub>, and (c) **3**. Conditions: frequency = 9.40 GHz, power = 10 mW, modulation frequency = 100 kHz, modulation amplitude = 20 G.

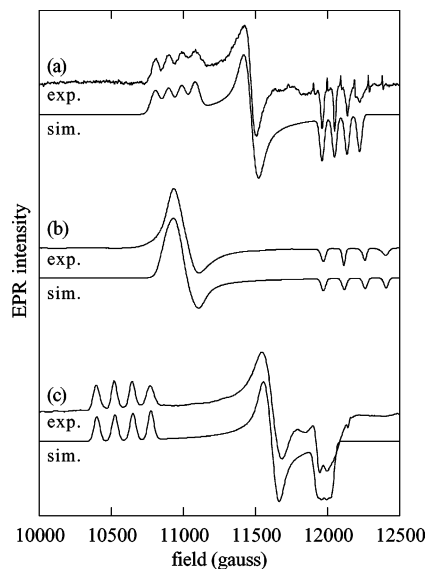


**Figure 5.** Experimental and simulated Q-band EPR spectra of frozen (77 K)  $\sim 1$  mM solutions of **1** in (a) toluene, (b) 9:1 toluene/1,4-dioxane, and (c) 99:1 toluene/pyridine. Conditions: frequency = 34.1 GHz, power = 0.32 mW, modulation frequency = 100 kHz, modulation amplitude = (a) 4 or (b and c) 20 G.

5c). The pattern of  $g$  values is again rhombic ( $g_1 \gg g_2 > g_3$ ), as it is in the toluene-only case, but the  $g$  values have changed significantly:  $g_1$  is much larger (2.297 vs 2.222),

**Table 1.** EPR Parameters for Frozen Solutions of **1**

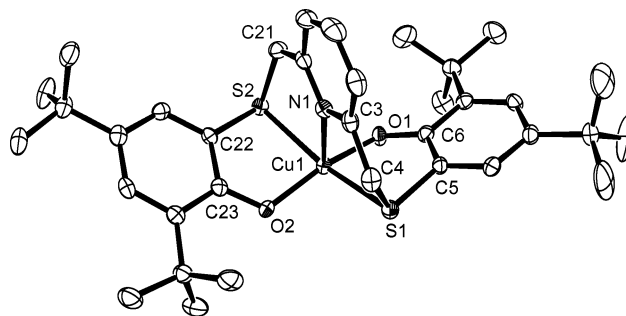
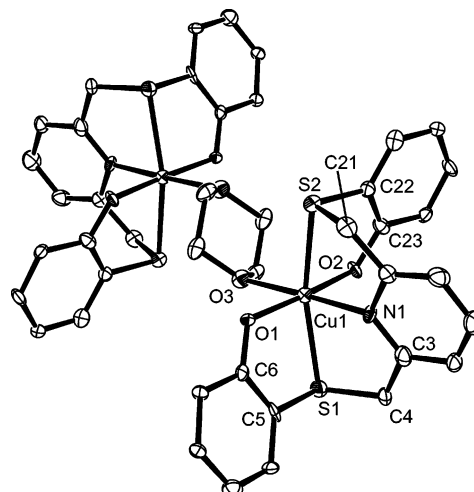
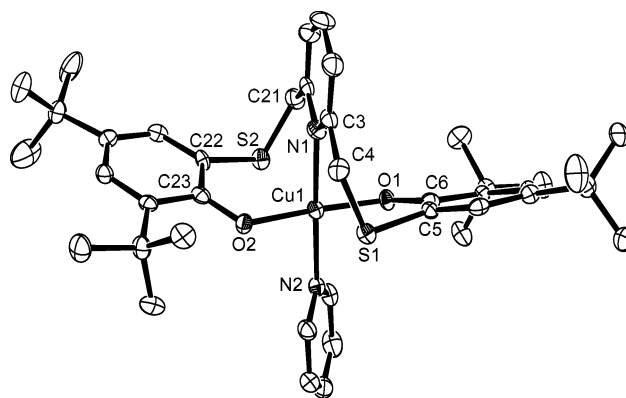
	solvent		
	toluene	toluene/dioxane	toluene/pyridine
$g_1$	2.222	2.205	2.297
$g_2$	2.120	2.205	2.095
$g_3$	2.011	1.997	2.030
$A_1$ (G)	92	40	125
$A_2$ (G)	—	40	25
$A_3$ (G)	87	145	35

and the difference between  $g_2$  and  $g_3$  is smaller ( $\Delta g = 0.06$  for **3** vs 0.11 for **1**). The spectrum is therefore more recognizable as a perturbation of a normal axial spectrum ( $g_1 \gg g_2 = g_3$ ). The lack of any residual unaffected signal of **1** indicates that formation of a new species is quantitative at low temperature.

Surprisingly, if an ether such as diethyl ether, tetrahydrofuran, 1,4-dioxane, or cyclohexene oxide is added to a solution of **1** in toluene (1–10% ether, v/v), the resulting frozen solution EPR spectrum exhibits an inverted axial pattern of  $g$  values ( $g_1 = g_2 > g_3$ ). The spectrum obtained for the 1,4-dioxane/toluene solution and simulations generated using the parameters given in Table 1 are shown in Figures 4b and 5b. The large shifts in the  $g$  values when compared with the toluene-only spectrum of **1** and the lack of signal due to residual **1** clearly indicate that dioxane binds to Cu quantitatively in the frozen solution, even though no UV–vis changes are seen in unfrozen solutions. If methanol (10–100%, v/v) is added to the toluene solution, the resulting spectrum appears to be a linear combination of the rhombic and inverted axial spectra, indicating that alcohols bond to **1**, but not quantitatively.

**X-ray Crystallography.** To further characterize some of the solvent adducts of **1**, crystals of its bridged 1,4-dioxane adduct **1**<sub>2</sub>(diox) (**2**) and pyridine adduct **1**(py) (**3**) were grown by evaporating solutions of **1** in water/organic solvent mixtures. Representations of the crystallographically determined structures of **1**·MeCN, **2**·(Me<sub>2</sub>CO)<sub>2</sub>, and **3** are shown in Figures 6–8, respectively (MeCN and Me<sub>2</sub>CO are solvents of crystallization and do not bind to Cu in **1** or **2**); crystallographic data and selected structural parameters are listed in Tables 2 and 3. In all cases, the ligand coordinates to Cu<sup>II</sup> in approximately square-pyramidal geometry with trans coordination of the phenolate O atoms and trans coordination of the thioether S atoms. In **1**, the S atoms are drawn toward the apical nitrogen, and the O atoms are pushed away, resulting in a tetrahedral distortion of the pyramidal base; the dihedral angle between the O(1)–Cu–S(1) and O(2)–Cu–S(2) planes is 11.5°. The remaining sixth coordination site is unoccupied in **1** and is occupied by an ethereal oxygen of 1,4-dioxane and the nitrogen of pyridine in **2** and **3**, respectively, completing distorted octahedral geometries about each metal center. The Cu–N and Cu–S distances of **1** are similar to those of a previously reported Cu–NS<sub>2</sub> pincer-type complex, although, in that case, the coordination sphere is instead completed by two chlorides rather than by chelating substituents on the pendant *S*-phenyl groups.<sup>23</sup>

The inclusion of 1,4-dioxane or pyridine in the coordination sphere is accompanied by adjustments of the chelating

**Figure 6.** ORTEP plot of **1**·MeCN shown with 50% probability ellipsoids. Hydrogen atoms and the uncoordinated MeCN molecule are omitted for clarity.**Figure 7.** ORTEP plot of **2**·(Me<sub>2</sub>CO)<sub>2</sub> shown with 50% probability ellipsoids. Hydrogen atoms, *tert*-butyl groups, and uncoordinated Me<sub>2</sub>CO molecules are omitted for clarity.**Figure 8.** ORTEP plot of **3** shown with 50% probability ellipsoids. Hydrogen atoms are omitted for clarity.

ligand. As the distance from copper to the exogenous ligand decreases from **1** to **2** to **3** (no ligand, 2.30 Å, 2.06 Å), the opposing Cu–N(1) distance also decreases (2.20, 2.18, 2.12 Å) whereas the Cu–S distances increase (mean = 2.40, 2.48, 2.62 Å). In comparison, the Cu–O distances are short and remain nearly constant (mean = 1.88, 1.89, 1.92 Å). Taken together, these parameters reflect an interesting reorientation of the Jahn–Teller distortion that is accommodated by the NO<sub>2</sub>S<sub>2</sub> ligand. The geometry about copper in five-coordinate **1** is roughly square pyramidal, with short Cu–O and Cu–S distances and N(1) occupying the axial position at an

**Table 2.** Crystallographic Data for **1**·MeCN, **2**·(Me<sub>2</sub>CO)<sub>2</sub>, and **3**

complex	<b>1</b> ·MeCN	<b>2</b> ·(Me <sub>2</sub> CO) <sub>2</sub>	<b>3</b>
formula	C <sub>37</sub> H <sub>50</sub> CuN <sub>2</sub> O <sub>2</sub> S <sub>2</sub>	C <sub>40</sub> H <sub>57</sub> CuNO <sub>4</sub> S <sub>2</sub>	C <sub>40</sub> H <sub>52</sub> CuN <sub>2</sub> O <sub>2</sub> S <sub>2</sub>
FW (g mol <sup>-1</sup> )	682.48	743.56	720.53
crystal system	monoclinic	triclinic	monoclinic
space group	<i>P</i> 2 <sub>1</sub> / <i>c</i> (No. 14)	<i>P</i> $\bar{1}$ (No. 2)	<i>P</i> 2 <sub>1</sub> / <i>c</i> (No. 14)
<i>a</i> (Å)	9.3310(1)	12.770(2)	10.9100(1)
<i>b</i> (Å)	17.7240(3)	13.517(2)	14.2681(2)
<i>c</i> (Å)	22.6640(1)	13.569(2)	24.5397(4)
$\alpha$ (deg)	90.00	99.592(3)	90.00
$\beta$ (deg)	98.900(1)	106.493(3)	98.456(1)
$\gamma$ (deg)	90.00	108.579(3)	90.00
volume (Å <sup>3</sup> )	3703.10(8)	2041.7(6)	3778.45(9)
<i>Z</i>	4	2	4
<i>T</i> (°C)	-142 ± 1	-141 ± 1	-104 ± 1
$\mu$ (Mo K $\alpha$ ) (cm <sup>-1</sup> )	7.35	6.75	7.24
$\rho_{\text{obs}}$ ( $\rho_{\text{calc}}$ ) (g cm <sup>-3</sup> )	(1.224)	(1.209)	(1.267)
crystal size (mm)	0.32 × 0.24 × 0.23	0.18 × 0.17 × 0.12	0.26 × 0.23 × 0.20
2 $\theta$ range (deg)	49.4	49.4	49.5
reflns collected	14576	10576	15860
unique reflns	5674	6520	5781
reflns with $F_o^2 > 4\sigma(F_o^2)$	4485	3153	4033
number of params	410	447	476
reflns/params ratio	13.84	14.59	13.26
$R^a$	0.036	0.079	0.048
$R_w^b$	0.095	0.180	0.121

<sup>a</sup>  $R = \sum||F_o| - |F_c||/\sum|F_o|$ . <sup>b</sup>  $R_w = [\sum(w(F_o^2 - F_c^2))/\sum w(F_o^2)]$ ,  $w = 1/[\sigma^2(F_o^2) + (0.0428P)^2 + 1.633P]$ ,  $P = (F_o^2 + 2F_c^2)/3$  for  $F_o^2 \geq 0$  and  $2F_c^2/3$  for  $F_o^2 < 0$ .

**Table 3.** Selected Bond Lengths (Å) and Angles (deg) for **1**·MeCN, **2**·(Me<sub>2</sub>CO)<sub>2</sub>, and **3**

	<b>1</b> ·MeCN	<b>2</b> ·(Me <sub>2</sub> CO) <sub>2</sub>	<b>3</b>
Cu(1)–O(1)	1.877(2)	1.885(4)	1.927(2)
Cu(1)–O(2)	1.878(2)	1.891(4)	1.904(2)
Cu(1)–S(1)	2.402(1)	2.467(2)	2.600(1)
Cu(1)–S(2)	2.399(1)	2.491(2)	2.632(1)
Cu(1)–N(1)	2.204(2)	2.175(5)	2.120(3)
Cu(1)–ligand	na	2.303(5)	2.064(3)
$\angle$ O(1)–Cu(1)–O(2)	162.9(1)	174.3(2)	176.7(1)
$\angle$ S(1)–Cu(1)–S(2)	162.8(1)	162.9(1)	160.8(4)
$\angle$ N(1)–Cu(1)–ligand	na	177.9(2)	176.9(1)

elongated distance. In **2**, Cu–O(1) and Cu–O(2) are short, whereas the four other distances are long, indicating relative axial compression along the O–Cu–O axis. Finally, the Cu–O and Cu–N distances in **3** are typical for a square-planar Cu<sup>II</sup> complex, whereas the Cu–S distances are long: the geometry is therefore axially elongated. Thus, Jahn–Teller distortion (either elongation or compression) can occur along each of the Cu–N(1), Cu–O, and Cu–S axes, as seen in **1–3**, respectively.

**Calculated Electronic Ground States.** Powder EPR spectra of the ground crystals of **1**·MeCN, **2**·(Me<sub>2</sub>CO)<sub>2</sub>, and **3** are included in Figure 4a–c. The samples are not magnetically dilute, so the signals are broadened and the hyperfine structure is not resolved. However, not only can differing patterns of *g* values be seen for **1**·MeCN (rhombic), **2**·(Me<sub>2</sub>CO)<sub>2</sub> (inverted axial) and **3** (near-axial), but these patterns also correlate with the patterns of the appropriate frozen solution spectra. Because of the good correlation of EPR powder spectra with the frozen solution spectra, the crystallographic coordinates of **1–3** were taken to be appropriate for single-point determinations of their electronic configurations by DFT calculations instead of attempting complete geometry optimizations. An extra check of the crystal structures for hidden disorder due to dynamic Jahn–

Teller distortions based on MSDA/TLS analysis showed no artifactual librational effects.<sup>29,30</sup> Two specific coordinate systems were fixed to allow quantitative comparisons of the ground-state configurations between the three structures: in *xyz* coordinates, the *z* axis lies along the Cu–S vectors, and in *x'y'z'* coordinates, the *z* axis lies along the Cu–N(1) vector (Figure 9).

For **1–3**, particular unoccupied  $\beta$ -MOs near the HOMO–LUMO gap are dominated by Cu-based contributions and appear to be the relevant unoccupied MOs.<sup>41</sup> Contour plots of these  $\beta$ -LUMOs are given in Figure 9. The easiest to describe is that of **3**, which is dominated by the  $d_{x^2-y^2}$  orbital of the Cu atom and antibonding interactions with the N and O atoms. Contributions from the axial sulfur atoms are insignificant, fully in line with the long Cu–S distances. The relevant  $\beta$ -LUMO of **2** appears to be  $d_{z^2}$  in character, but the coordinate systems dictate that it is either  $d_{x^2}$  (*xyz* coordinates) or  $d_{x'^2}$  (*x'y'z'* coordinates). The longer Cu–N(1) and Cu–L distances relative to those in **3** are reflected by visibly smaller contributions from the ether and pyridine moieties. Also, unlike in **3**, sulfur atomic orbitals contribute noticeably to the relevant  $\beta$ -LUMO of **2**. The  $\beta$ -LUMO of **1** is similar to that of **2**, but if compared closely, it is distorted away from a simple  $d_{z^2}$  shape. A larger sulfur contribution to the ground state can be discerned, and there appears to be little interaction with the pyridine moiety.

Quantitative evaluations of the atomic orbital contributions to the relevant  $\beta$ -LUMOs of **1–3** in both coordinate systems are summarized in Table 4. The most important trend to note is in the balance of  $d_{x^2-y^2}$  and  $d_{z^2}$  contributions in **1–3**, as these contributions directly impact the *g* values of the EPR spectra (vide infra). A decreasing balance of  $d_{z^2}$  character on proceeding from **1** to **3** in the *xyz* coordinate system is

(41) McGarvey, B. R. *Trans. Met. Chem.* **1966**, *3*, 89–201.

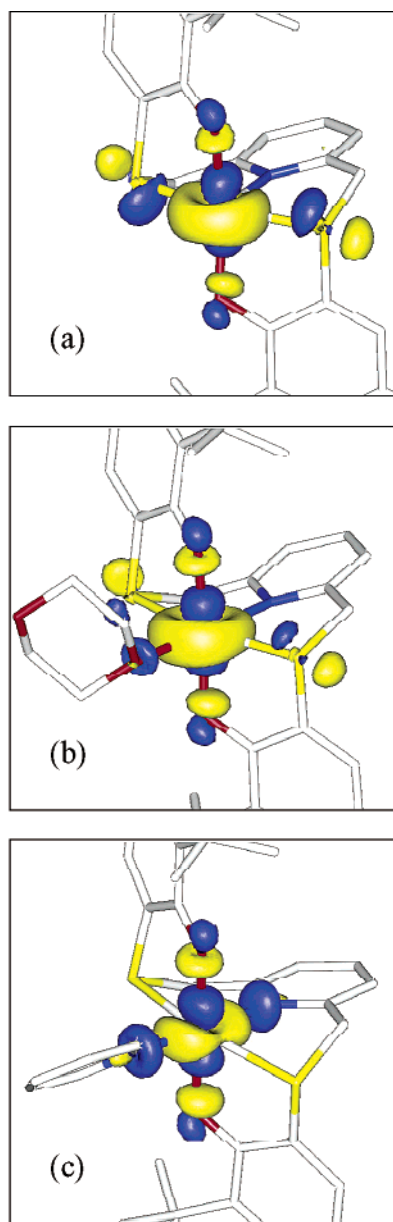


**Figure 9.** MO contour plots containing 95% of the electron density for the relevant  $\beta$ -LUMOs of (a) **1**, (b) **2** (mononuclear), and (c) **3**. Also shown are schemes of the  $xyz$  and  $x'y'z'$  coordinate systems coinciding with the molecular axes that were used to determine the d-orbital contributions to the  $\beta$ -LUMOs.

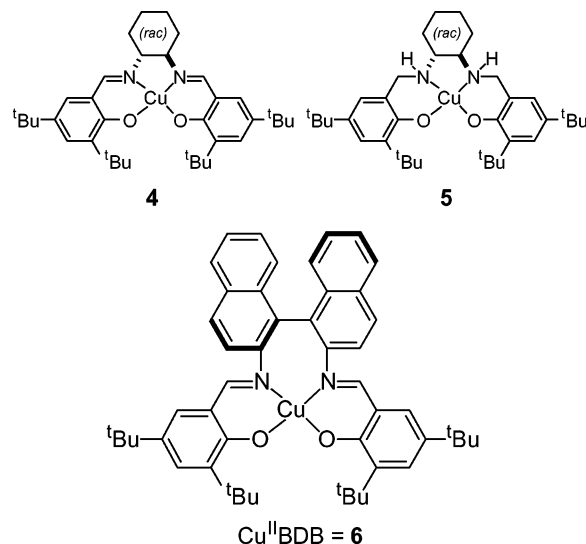
mirrored by a trend of increasing  $d_{z^2}$  character in the  $x'y'z'$  calculations. The orbital energies and total contributions from the Cu, O, and S orbitals are identical, as these are independent of direction. The reduced Cu–S interaction perceived in the MO contour plots of **2** and **3** when compared to that of **1** is also quantified as a reduction of the S character from 13% in **1** to 11% in **2** and to 2% in **3**.

**Table 4.** Calculated Compositions of Relevant  $\beta$ -LUMOs of **1–3**

	$xyz$ coordinates <sup>a</sup>			$x'y'z'$ coordinates <sup>b</sup>		
	<b>1</b>	<b>2</b>	<b>3</b>	<b>1</b>	<b>2</b>	<b>3</b>
$E$ (eV)	−0.80	−0.16	0.35	−0.80	−0.16	0.35
Cu (total)	70	75	76	70	75	76
S (total)	13	11	2	13	11	2
O (total)	5	6	8	5	6	8
$d_{x^2-y^2}$ (%)	27	52	72	57	50	30
$d_{z^2}$ (%)	31	16	2	4	18	45
$d_{xy}$ (%)	3	1	0	0	0	0
$d_{xz}, d_{yz}$ (%)	0	0	1	0	0	0
$b^2 c$	0.53	0.24	0.03	0.06	0.27	0.60

<sup>a</sup>  $xyz$ :  $xy = \text{Cu}-\text{NO}_2$ ,  $z \approx \text{Cu}-\text{S}$ . <sup>b</sup>  $x'y'z'$ :  $z' = \text{Cu}-\text{N}$ ,  $x'y' = \text{Cu}-\text{O}_2\text{S}_2$ . <sup>c</sup> Based on percent  $d_{x^2-y^2}$  and percent  $d_{z^2}$  only.

**Chart 1**



## Discussion

The thioethers contained in the ligand **H<sub>2</sub>L1** were intended to serve a dual role: to donate electron density to the phenolate rings, thereby lowering the potentials for phenoxyl formation, and to bond to copper, thereby favoring reduction to a Cu<sup>I</sup> state. When compared to complexes **4** and **5** that we studied previously (Chart 1), the redox potentials of **1** are about equal to those of **4** and significantly higher than those of **5**, which suggests that the sulfur substituents behave as electron-withdrawing groups.<sup>15</sup> The crystal structure of **1**·MeCN shows that the occupied, electron-donating sulfur p orbitals are aligned to bond to the copper center instead of  $\pi$  conjugating with the phenolates. The high potentials of **1** probably also contribute to its instability when oxidized, as a strong thermodynamic driving force for decomposition exists in [**1**]<sup>+</sup>. Copper complexes of other chelating *ortho*-sulfanylphenolate ligands were reported to be irreversibly oxidized.<sup>18</sup>

The reduction process of **1** that is assigned to a Cu<sup>II</sup>/Cu<sup>I</sup> couple is preceded in GOase model studies: **6** (Chart 1), the copper complex of a binaphthyl-salen-like ligand, has reversible, ligand-based oxidations and a Cu<sup>II</sup>/Cu<sup>I</sup> couple at −1400 mV vs Fc<sup>+</sup>/Fc in MeCN.<sup>42</sup> In the salen-like case, stabilization of a Cu<sup>I</sup> form results from tetrahedral proclivity

(42) Wang, Y. Ph.D. Thesis, Stanford University, Stanford, CA, 1998.

of the coordination sphere induced by the seven-membered chelate ring formed with the binaphthylidiamine backbone. In the case of **1**, a large peak-to-peak separation for the reduction (Figure 2) suggests that some rearrangement occurs upon reduction and reoxidation.<sup>38</sup> The O<sub>2</sub>S<sub>2</sub> plane in the crystal structure of **1**·MeCN is itself tetrahedrally distorted, so it seems possible that, upon reduction, the Cu–N(1) distance would extend further and the phenolates would rotate to achieve a more tetrahedral geometry. Alternatively, loss of the nitrogen and sulfur donors could result in a linear complex coordinated by the phenolate oxygens. Either of these geometries is favorable for Cu<sup>I</sup> complexes, although they are speculative and other geometries are certainly possible.

The difficulties of stabilizing oxidized and reduced forms of **1** prevent investigations of their properties as spectroscopic or functional models of GOase. Inclusion of groups more electron-donating than the *tert*-butyl substituents on the phenolates could lower the oxidation potentials and stabilize the phenoxyl form; however, the increased electron density would probably also make the Cu<sup>II</sup>/Cu<sup>I</sup> potential lower. Therefore, although the design of **1** improves over the complete lack of an observable Cu<sup>I</sup> form of the salen complexes **4** and **5**, there is still a 1700-mV thermodynamic gap between its putative active forms. In contrast, the potentials for oxidation and reduction of GOase<sub>semi</sub> to GOase<sub>ox</sub> and GOase<sub>red</sub> are estimated to be 400 and 150 mV vs NHE, respectively, creating only a 250-mV thermodynamic gap.<sup>3</sup> Comparison of the Cu<sup>II</sup>/Cu<sup>I</sup> reduction potentials must acknowledge that GOase is studied in buffered aqueous media, and the protons available from the media can stabilize GOase<sub>red</sub> by protonating the tyrosine residues and attenuating their anionic charge. Meaningful studies of **1** in proton-containing nonaqueous media, however, are difficult to envisage.

Taken as subjects of coordination chemistry, **1** and its derivatives demonstrate that the ligand **L1**<sup>2-</sup> provides a unique coordination environment for copper. Beyond the interesting spectra that **1** and its derivatives supply, there is a conundrum in determining why the EPR spectrum of **1** appears to be intermediate between those of **2** and **3**. It would seem more logical for the EPR spectrum of **1** appears to be intermediate between those of **2** and **3**. It would seem more logical for the EPR spectrum of **1** appears to be intermediate between those of **2** and **3**. In low-symmetry complexes such as **1–3**, the usual d<sub>x<sup>2</sup>-y<sup>2</sup></sub> Cu<sup>II</sup> ground state can mix and gain d<sub>z<sup>2</sup></sub> character. The expressions for the *g* values of a  $\Psi = ad_{x^2-y^2} + bd_{z^2}$  ground state ( $a^2 + b^2 = 1$ ) derived by perturbation theory are

$$g_x = 2.00 - \frac{2k_x^2\lambda(a - \sqrt{3}b)^2}{E_{xz}}$$

$$g_y = 2.00 - \frac{2k_y^2\lambda(a + \sqrt{3}b)^2}{E_{yz}}$$

$$g_z = 2.00 - \frac{8k_z^2\lambda a^2}{E_{xy}}$$

where *k* is a covalency reduction factor,  $\lambda$  is the inherent

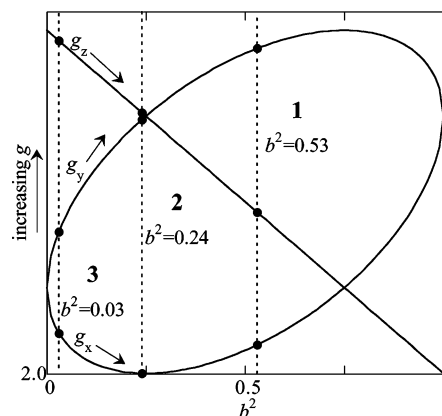


**Figure 10.** Qualitative plot of  $g_x$ ,  $g_y$ , and  $g_z$  as functions of  $b^2$ , the fractional  $d_{z^2}$  character in the ground-state wave function. Predicted patterns of  $g$  values are shown for **1–3** based on the computed composition of their relevant  $\beta$ -LUMOs in the  $xyz$  coordinate system (Table 4).

spin–orbit coupling constant of Cu<sup>II</sup> (approximately  $-830 \text{ cm}^{-1}$ ), and  $E_{ij}$  is the d–d transition energy from the  $d_{ij}$  orbital to the  $d_{x^2-y^2}/d_{z^2}$  orbital.<sup>41,43</sup> Changes in  $E_{ij}$  are relatively small in traditional Cu<sup>II</sup> complexes; it is the  $d_{z^2}$  character of  $\Psi(b)$  that drives rhombic splitting of  $g_x$  and  $g_y$  because of the sign change from  $-\sqrt{3}b$  to  $+\sqrt{3}b$  in their expressions. If plotted as a function of  $b^2$  (i.e.,  $d_{z^2}$  character) holding  $k$  and  $E_{ij}$  constant, the three  $g$  values give the elliptical plot in Figure 10. As the  $g$ -value expressions are derived from perturbation theory, this plot is difficult to justify quantitatively for large values of  $b^2$  ( $>0.25$ ), but it is useful for qualitative evaluation of the DFT computational results. For **1–3**, the calculated values of  $b^2$  in the  $xyz$  coordinate system are 0.53, 0.24, and 0.03, respectively. Judging from these values, the  $g$ -value plot correctly predicts EPR spectra that are rhombic ( $g_y > g_z > g_x$ ) for **1**, inverted axial ( $g_z \approx g_y \gg g_x$ ) for **2**, and slightly rhombic ( $g_z \gg g_y > \approx g_x$ ) for **3**. The apparent intermediacy of the EPR spectrum of **1** between those of **2** and **3** arises because  $g_z$  for **1** is smaller than  $g_y$ , indicating that, whereas  $xyz$  is an adequate coordinate system for describing the ground states of **2** and **3**, it describes the ground state of **1** poorly. In the  $x'y'z'$  coordinate system, the  $g_y$  and  $g_z$  values for **3** are inverted, similarly indicating that  $x'y'z'$  is a poor system for describing the ground state of **3**. However, if **1–3** are to be simultaneously described as a series, this difficulty can be accommodated by these awkward linear combinations of the d orbitals.

The EPR spectrum of GOase<sub>semi</sub> shows the axial pattern of a  $d_{x^2-y^2}$  ground state, and superhyperfine coupling to two nitrogens strongly suggests that both His496 and His581 must occupy the  $xy$  plane.<sup>44</sup> However, in GOase<sub>ox</sub>, antiferromagnetic coupling of Cu<sup>II</sup> with the protein-derived radical

(43) These expressions summarize first-order effects only and cannot account for the  $g_z$  value less than 2.00 of **2**. If the first-order perturbation is small, d-orbital-based second-order effects can decrease a  $g$  value to slightly below 2.00. Also, ligand-based spin–orbit coupling can have significant effects if the ligating atom is from the third-row elements and beyond. In the ground state of **2**, there is a significant amount of sulfur character. Because the spin–orbit coupling constant of sulfur is  $\sim 380 \text{ cm}^{-1}$  (i.e., large and positive), the  $g$  values would decrease.

(44) Bereman, R. D.; Kosman, D. J. *J. Am. Chem. Soc.* **1977**, *99*, 7322–7325.

prevents experimental determination of the ground-state configuration.<sup>2</sup> Despite contrary claims based on computational studies,<sup>45,46</sup> experimental evidence is most consistent with the modified tyrosinate (Tyr272) being the locus of the radical.<sup>47,48</sup> If, as is usually proposed, the axial tyrosine (Tyr495) is deprotonated in GOase<sub>ox</sub>, it would serve as a strongly anionic donor, compensating for the weak equatorial tyrosyl ligand. The effects of this strong axial–weak equatorial coordination might include mixing of the Cu<sup>II</sup> d manifold in an adjustment of the ground-state wave function, but the potential consequences for enzyme function (e.g., stabilization of the oxidized form, prevention of side reac-

tions) are unclear. The impact on the reaction mechanism of GOase is likely minimal, as alcoholic substrates are proposed to transfer protons to Tyr495 and bond to Cu as anions, unequivocally defining the equatorial plane.

**Acknowledgment.** This work was supported by funding from the NIH (GM50730) and an Urbanek Family Stanford Graduate Fellowship (R.C.P.). We thank Professor E. I. Solomon for helpful discussions and the use of EPR and UV–vis–NIR instruments, P. Chen for helpful discussions regarding DFT methods, and L. Quintanar for assistance with acquisition of Q-band EPR spectra. We thank a reviewer for suggesting the thermal analyses.

**Supporting Information Available:** Full crystallographic reports with appropriate metrical tables in text and CIF formats for **1**·MeCN, **2**·(Me<sub>2</sub>CO)<sub>2</sub>, and **3** and MSDA analyses of their copper coordination spheres. This information is available free of charge via the Internet at <http://pubs.acs.org>.

IC048904Z

- (45) Rothlisberger, U.; Carloni, P. *Int. J. Quantum Chem.* **1999**, *73*, 209–218.  
(46) Himo, F.; Eriksson, L. A.; Maseras, F.; Siegbahn, P. E. M. *J. Am. Chem. Soc.* **2000**, *122*, 8031–8036.  
(47) Babcock, G. T.; Eldeeb, M. K.; Sandusky, P. O.; Whittaker, M. M.; Whittaker, J. W. *J. Am. Chem. Soc.* **1992**, *114*, 3727–3734.  
(48) Whittaker, M. M.; Chuang, Y. Y.; Whittaker, J. W. *J. Am. Chem. Soc.* **1993**, *115*, 10029–10035.